Understanding How Processing Additives Tune the Nanoscale Morphology of High Efficiency Organic Photovoltaic Blends: From Casting Solution to Spun-Cast Thin Film

*Ming Shao, Jong Kahk Keum, Rajeev Kumar, Jihua Chen, James F. Browning, Sanjib Das, Wei Chen, Jianhui Hou, Changwoo Do, Kenneth C. Littrell, Adam Rondinone, David B. Geohegan, Bobby G. Sumpter, and Kai Xiao**

Adding a small amount of a processing additive to the casting solution of photoactive organic blends has been demonstrated to be an effective method for achieving improved power conversion efficiency (PCE) in organic photovoltaics (OPVs). However, an understanding of the nano-structural evolution occurring in the transformation from casting solution to thin photoactive films is still lacking. In this report, the effects of the processing additive diiodooctane (DIO) on the morphology of the established blend of PBDTTT-C-T polymer and the fullerene derivative $PC_{71}BM$ used for OPVs are investigated, starting in the casting solution and tracing the effects in spun-cast thin films by using neutron/X-ray scattering, neutron reflectometry, and other characterization techniques. The results reveal that DIO has no observable effect on the structures of PBDTTT-C-T and $PC_{71}BM$ in solution; however, in the spun-cast films, it significantly promotes their molecular ordering and phase segregation, resulting in improved PCE. Thermodynamic analysis based on Flory-Huggins theory provides a rationale for the effects of DIO on different characteristics of phase segregation due to changes in concentration resulting from evaporation of the solvent and additive during film formation. Such information may help improve the rational design of ternary blends to more consistently achieve improved PCE for OPVs.

1. Introduction

Organic photovoltaics (OPVs) based on blends of electron-donating conjugated polymers and electron-accepting fullerene derivatives have attracted tremendous attention as low-cost and renewable next-generation energy sources. Remarkable progress has been made in improving the power conversion efficiency (PCE) of OPVs above 11% by a combination of new materials synthesis, morphology optimization and advanced device engineering.[1,2] For high efficiency solar cells, conjugated polymers are required to have a broad light absorption spectrum that effectively overlaps the solar spectrum for effective exciton generation, and high charge carrier mobility for efficient charge transport and collection. In order to meet these criteria, much effort has been expended to synthesize new conjugated polymers, in particular low band gap polymers.[3,4] Also, the PCE of an OPV device strongly depends on the nanoscale morphology of the electron donor (ED) and acceptor (EA) in the active layer.[5] The ideal morphology has been postulated to be the bulk heterojunction (BHJ), where the ED and EA form a nanoscale bicontinuous network. This nanoscale network ensures short path lengths for exciton diffusion, large interfacial area between ED and EA for effective exciton separation, and sufficient network connectivity pathways for effective charge transport and collection. To achieve different BHJ morphologies, a variety of processing techniques have been explored such as

Dr. M. Shao, Dr. J. K. Keum, Dr. R. Kumar, Dr. J. Chen, Dr. A. Rondinone, Dr. D. B. Geohegan, Dr. B. G. Sumpter, Dr. K. Xiao
Center for Nanophase Materials Sciences
Oak Ridge National Laboratory
Oak Ridge, TN 37831, USA
E-mail: xiaok@ornl.gov

Dr. J. K. Keum, J. F. Browning, C. Do, K. C. Littrell
Neutron Scattering Science Divisions
Oak Ridge National Laboratory
Oak Ridge, TN 37831, USA

Dr. R. Kumar, B. G. Sumpter
Computer Science and Mathematics Division
Oak Ridge National Laboratory
Oak Ridge, TN 37831, USA

DOI: 10.1002/adfm.201401547

S. Das
Department of Electrical Engineering and Computer Science
University of Tennessee
Knoxville, TN 37996, USA

Dr. W. Chen
Material Sciences Division
Argonne National Laboratory
Argonne, Illinois 60439, USA

Dr. J. Hou
Institute of Chemistry
Chinese Academy of Sciences
Beijing 10080, China

annealing films by directly heating[5,6] or heating with solvent vapor,[7] using solvent mixtures,[8,9] or by using additives such as small molecules,[10] polymers,[11,12] inorganic nanocrystals,[13] and high boiling solvents.[14] Among these strategies, adding small amounts of a processing additive (PA) in addition to the primary host solvent has been found widely effective for BHJ morphology control while maintaining compatibility with large-scale processing techniques.[14–16] Moreover, no additional thermal or solvent vapor annealing is necessary when processing additives are used.[3,17] Various functional PAs, such as 1,8-octanedithiol (ODT),[15] 1,8-diiodooctane (DIO),[3,14] and 1-chloronaphthalene (CN),[16] have been demonstrated to alter BHJ morphologies and improve OPV efficiencies.

However, due to the lack of direct characterization of the nanoscopic and mesoscopic film morphology, the causal mechanisms of solvent additives on BHJ morphology responsible for the improved OPV efficiencies remains poorly understood. Improvements in BHJ morphology usually result from either the self-organization of the polymer donor into more ordered structures or the aggregation of fullerene acceptor domains into more favorable percolating networks for exciton dissociation and transport. In general, most previous studies have agreed that solvent PA's increase the overall crystallinity or modify the size of crystalline domains of the conjugated polymer donor. However, differing observations have been reported regarding the change in the size of the fullerene acceptor domains (both increasing and decreasing) upon adding various solvent additives in different donor-acceptor blends.[3,13,14] For example, the Heeger group[14] found that the solvent additive ODT can promote the aggregation of fullerene-rich domains in PCPB-DTBT/PCBM BHJ films while Liang et al.[3] observed that the solvent additive DIO reduces oversized fullerene rich domains (from ~ hundreds of nanometers to tens of nanometers) in PTB7/PCBM BHJ films. Moreover, crucial information about the structural evolution of the polymer donor and the fullerene acceptor from the initial blend in the solution state to the final BHJ morphology in the film state has not been thoroughly investigated. Only recently Lou[18] and Schmidt[19] reported small-angle X-ray scattering (SAXS) results for conjugated polymer:$PC_{71}BM$ blend solutions, whereby it was proposed that the added DIO selectively increases the solubility for $PC_{71}BM$ when mixed with host chlorobenzene (CB) solvent. Based on the SAXS results that showed that DIO reduced the aggregate size of $PC_{71}BM$ in the casting solution, the authors concluded that improvements in the PCE of the OPV device resulted from reduced domain sizes of $PC_{71}BM$ in the spun-cast active layer.

In ternary OPV blend solutions consisting of a conjugated polymer, a fullerene derivative and a solvent, two scattering length density (SLD) contrasts are generally dominant in SAXS: that between the conjugated polymer and the solvent, and that between the fullerene derivative and the solvent. However, multiple scattering signals originate from the different materials, making it very difficult to interpret the scattering result unambiguously. In this regard, small-angle neutron scattering (SANS) is a very powerful complementary tool to SAXS, since the contrast-matching capability of SANS can make it possible to remove one of the SLD contrasts by matching the SLDs between one of the blend components and the solvent to identify the structure of the other component with reduced ambiguity. Adjusting the SLD contrast to the second blend component can similarly reveal the structure of the first. However, despite this versatility, SANS has not been extensively applied to study the morphologies of polymer blends in solution or to follow the role of PA's in the resulting film morphologies. It is highly likely that the structures of electron donor and acceptor complexes in spin-casting solutions could affect the morphology of the BHJ formed in the spun-cast active layer. However, a systematic study of ED and EA morphology from solution to thin film for OPV blends is quite rare.

Hence, in this work, we focus on understanding the structural and morphological evolution of polymer/PCBM blends occurring from the casting solution to spun-cast thin film, both with and without a processing additive. Binary blends of a low band gap conjugated polymer, PBDTTT-C-T, and the fullerene derivative $PC_{71}BM$ are chosen as a model blend system for this study. The processing additive 1,2-diiodooctane (DIO) is chosen for this blend since this system has been previously reported to result in a high OPV efficiency of 7.59%.[4] Small-angle neutron scattering, small-angle x-ray scattering, neutron reflectometry (NR) and other characterization tools are employed to understand the effects of processing additives on BHJ morphological variations at various length scales. The structural evolution from casting solution to spun-cast film is examined to provide insight into the interaction among BHJ blending materials, host solvents, and additives during processing. The results reveal that the added DIO has no effect on the solution structures of PBDTTT-C-T and $PC_{71}BM$, but does significantly promote the molecular ordering and phase segregation of PBDTTT-C-T and $PC_{71}BM$ in the spun-cast film, which subsequently leads to an improved PCE. A phase diagram constructed using Flory-Huggins theory provides a rationale for the effects of the DIO and the solvent on the different characteristics of phase segregation. Correlating this structural information with the improved PCE can provide a framework to rationally guide the choice of different materials and the design of different processing strategies.

2. Results and Discussion

Figure 1a shows the current (J)–voltage (V) curves for the PBDTTT-C-T:$PC_{71}BM$ OPVs, in which the active layers were spun-cast from solutions of 1:1.5 wt% PBDTTT-C-T:$PC_{71}BM$ in either pure 1,2-dichlorobenzene (DCB) or DCB with 3 wt% DIO as a processing additive. The associated device parameters such as short-circuit current (J_{sc}), open circuit voltage (V_{oc}), fill factor (FF) and power conversion efficiency (PCE) are tabulated in **Table 1**. In the films with DIO, J_{sc} is increased from 12.97 to 15.74 mA/cm^2 and the FF increases from 42.23 to 57.15%, which leads to an ≈36% enhancement of PCE from 4.52 to 7.12%. On the contrary, there is a small reduction of V_{oc} from 0.825 to 0.791 V, suggesting that ordering of the active layer is induced by DIO, which is usually favorable for charge transport.[15,20,21] Figure 1b shows the EQE curves of the PSCs fabricated under the same optimized conditions as those used for the J–V measurements. Obviously, the EQE value for PBDTTT-C-T with the additive DIO is higher than that of PBDTTT-C-T without it, which agrees with the similarly higher J_{sc} values of the devices.

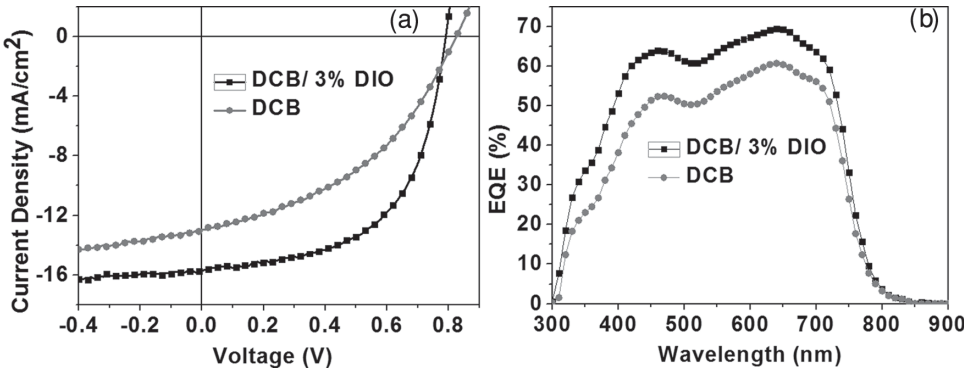

Figure 1. a) *J–V* curves of the polymer solar cells based on PBDTTT-C-T/PCBM with and without a DIO additive under illumination of AM 1.5G, 100 mW cm^{-2}. b) EQE curves of the corresponding polymer solar cells.

In order to investigate the morphological origins for the improved PCE, we first conducted SANS measurements for the PBDTTT-C-T:$PC_{71}BM$/DCB and PBDTTT-C-T:$PC_{71}BM$/DCB:DIO solutions. In the solutions, three different phases with different SLDs, i.e., PBDTTT-C-T, $PC_{71}BM$, and DCB (or DCB/DIO) phase exist yielding multiple scattering signals. The coexistence of scattering signals originating from the two different SLD contrasts between PBDTTT-C-T and solvent, and $PC_{71}BM$ and solvent, make it difficult to resolve the multiple scattering and interpret the SANS data. Hence, contrast matching methods of SANS are utilized to resolve the SANS signals, and identify the structures of each blending component. Contrast matching is implemented by adjusting the composition of deuterated-DCB (*d*-DCB) and DCB to match the SLD with that of $PC_{71}BM$. Here, the 94:6 vol% solvent mixture of *d*-DCB and DCB that is SLD-matched to that of $PC_{71}BM$ is denoted as *m*-DCB. The SLDs of PBDTTT-C-T, $PC_{71}BM$, DCB, and DIO are 1.00×10^{-6}, 4.34×10^{-6}, 2.35×10^{-6}, and 0.12×10^{-6} Å^{-2}, respectively, see Table S1 (Supporting Information), where the SLDs of PBDTTT-C-T and $PC_{71}BM$ are obtained from neutron reflectivity measurements as shown in Figure 5, and those of DIO, deuterated (*d*-) DCB, and DCB are calculated based on the mass densities and neutron scattering lengths.[22] In the SANS measurements for the PBDTTT-C-T:$PC_{71}BM$/m-DCB and PBDTTT-C-T:$PC_{71}BM$/m-DCB:DIO solution, only the scattering signal associated with the structure of PBDTTT-C-T will be detected while no signal with respect to $PC_{71}BM$ is expected due to the zero SLD contrast between $PC_{71}BM$ and solvents. Also, by varying the SLD of the solvent and comparing the resultant scattering curves, the structure of $PC_{71}BM$ could be determined. **Figure 2**a,b shows the experimental SANS curves for various solutions, where the markers are as indicated. In Figure 2a, the solid lines denote the results of model fits based on a flexible cylinder model[23,24] and the fit parameters are summarized in **Table 2**. In Figure 2a,b, the SANS curves of *m*-DCB/DIO and DCB/DIO merely exhibiting flat scattering features imply a good miscibility between the host solvents and DIO. SANS curves for $PC_{71}BM$/DCB, $PC_{71}BM$/DCB/DIO, $PC_{71}BM$/*m*-DCB and $PC_{71}BM$/*m*-DCB/DIO solution are also collected to examine how $PC_{71}BM$ exists in DCB and DCB/DIO. Due to the matching SLD between $PC_{71}BM$ and *m*-DCB, and $PC_{71}BM$ and *m*-DCB:DIO, the SANS curves of $PC_{71}BM$/*m*-DCB and $PC_{71}BM$/*m*-DCB/DIO solution exhibit flat scattering feature. Like those of $PC_{71}BM$/m-DCB and $PC_{71}BM$/m-DCB/DIO solution, the SANS curves of $PC_{71}BM$/DCB and $PC_{71}BM$/DCB/DIO solution also show flat scattering features, indicating a complete dissolution of $PC_{71}BM$ in DCB and DCB/DIO. If $PC_{71}BM$ forms aggregates or clusters in the solution, scattering patterns showing asymptotic decays in scattered intensity should be observed. The SANS results exhibiting the complete dissolution of PBDTTT-C-T and $PC_{71}BM$ in DCB are consistent with the thermodynamic analysis study that will be discussed later. Lou et al. has reported that $PC_{71}BM$ forms aggregates in conjugated polymer/$PC_{71}BM$/chlorobenzene solution, while the size of $PC_{71}BM$ aggregates are reduced by adding small amounts of DIO.[18] The reduced size of $PC_{71}BM$ aggregates was proposed to be due to DIO acting as a good solvent for $PC_{71}BM$. Based on this observation, the authors suggested that the different initial morphologies of $PC_{71}BM$ in the casting solutions subsequently result in different phase morphologies in the spun-cast thin films.[18] As will be shown later, however, the solubility parameters of PBDTTT-C-T, $PC_{71}BM$, DIO and DCB indicate that DIO is a poorer solvent than DCB for PBDTTT-C-T and $PC_{71}BM$. The effect of DIO on the chain conformation of PBDTTT-C-T can also be found by comparing the SANS data for PBDTTT-C-T/*m*-DCB, PBDTTT-C-T/*m*-DCB/DIO, PBDTTT-C-T/$PC_{71}BM$/*m*-DCB and PBDTTT-C-T/$PC_{71}BM$/*m*-DCB/DIO, where the SANS curves are modeled using a flexible cylinder model.[23,24] In the blend solutions of PBDTTT-C-T/$PC_{71}BM$/*m*-DCB and PBDTTT-C-T/$PC_{71}BM$/*m*-DCB/DIO, since *m*-DCB is used to match its SLD with that of $PC_{71}BM$, the collected SANS signals are purely associated with the structure of PBDTTT-C-T chains as are those in PBDTTT-C-T/m-DCB and PBDTTT-C-T/m-DCB/DIO. In Figure 2a and Table 2, the collected SANS data for different solutions exhibit identical scattering features with the identical model fit parameters, such as contour length, Kuhn length and lateral diameter within the error ranges. This means that the chain conformation

Table 1. Summary of J_{sc}, V_{oc}, FF and PCE for the OPV devices.

Device	J_{sc} [mA cm^{-2}]	V_{oc} [V]	FF [%]	PCE [%]
DCB	12.97	0.825	42.23	4.52
DCB/ 3%DIO	15.74	0.791	57.15	7.12

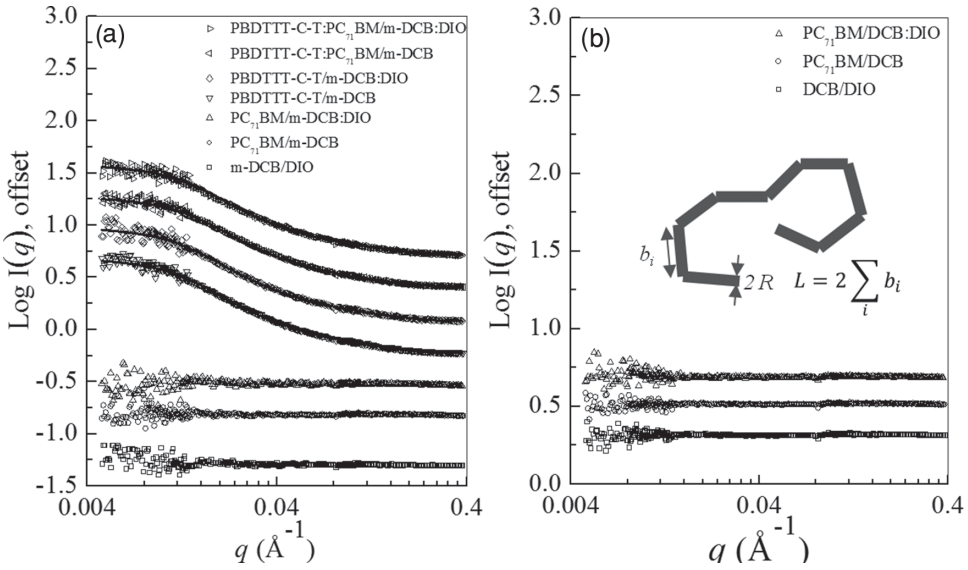

Figure 2. Small-angle neutron scattering (SANS) curves for the various solutions, where the markers are as indicated. a) Solid lines imply the model-fits based on the flexible cylinder model as depicted in the inset of (b) and described in the Supporting Information. Fit model parameters, such as contour length (*L*), Kuhn segmental length (*b*), radius (R) and the polydispersity in radius were shown in Table 2.

of PBDTTT-C-T is not influenced by the added DIO. The results also indicate that $PC_{71}BM$ does not affect the structure of PBDTTT-C-T at such a dilute concentration. Based on the SANS results indicating no effect of DIO in the solution structures of PBDTTT-C-T and $PC_{71}BM$, we hypothesize that the improved PCE is due to different morphological evolution in the blend films induced by DIO.

In an effort to verify this hypothesis, PBDTTT-C-T:$PC_{71}BM$/DCB and PBDTTT-C-T:$PC_{71}BM$/DCB:DIO solutions were spun-cast onto Si-substrates to prepare thin films and the films were examined using UV-Vis spectroscopy. Figure S1 compares the UV-Vis absorption spectra for the PBDTTT-C-T:$PC_{71}BM$/DCB and PBDTTT-C-T:$PC_{71}BM$/DCB:DIO films, which are spun-cast from PBDTTT-C-T:$PC_{71}BM$/DCB and PBDTTT-C-T:$PC_{71}BM$/DCB:DIO solutions. As seen in Figure S1 (Supporting Information), PBDTTT-C-T exhibits strong absorption peaks at 550–750 nm, whereas the $PC_{71}BM$ shows the peaks at ≈375 and 470 nm. Comparing the absorption spectra indicates a clear red-shift occurred due to the addition of DIO. The red-shift suggests that the added DIO facilitates an improved molecular packing of PBDTTT-C-T.

Two-dimensional (2D) grazing-incidence wide-angle X-ray scattering (GIWAXS) was used to obtain insights into the global orientation, molecular packing and crystallinity of PBDTTT-C-T and $PC_{71}BM$ in a thin film. The 2D GIWAXS pattern for the PBDTTT-C-T film is shown in **Figure 3**a. The in-plane and out-of-plane scattering profile, that is, I (q_y) versus q_y and I (q_z) versus q_z are extracted from the 2D pattern and depicted in Figures 3d,e, respectively. Here, q_y and q_z are the in-plane and out-of-plane scattering vectors, respectively. In the 2D GIWAXS pattern, the reflection arc discerned at q_y = 0.283 Å^{-1} (*d*-spacing = 22.2 Å), corresponds to (100) planes of the PBDTTT-C-T crystal. A broad out-of-plane reflection arc is also observed at q_z = 1.56 Å^{-1} (*d*-spacing = 4.03 Å), which is associated with the (010) reflection of the PBDTTT-C-T crystal. These in-plane (100) and out-of-plane (010) reflections indicate that the planes of PBDTTT-C-T aromatic backbones are predominantly aligned parallel to the surface plane of substrate with the alkyl side chains directed toward the in-plane direction. This orientation is the so-called face-on orientation of PBDTTT-C-T crystals that is desired for efficient charge transport in BHJ OPVs. In the 2D patterns of the blend films as shown in Figure 3b,c, the observed (100) reflection rings imply a random orientation of crystals. On the other hand, the broad reflection halos centered at q ≈ 1.37 Å^{-1} (*d*-spacing = 4.59 Å) are attributed to the random orientation and short range ordering of aggregated $PC_{71}BM$, that is, the (311) reflection of $PC_{71}BM$ crystal, as shown in Figure 3f. The most notable scattering feature

Table 2. Parameters used to fit the SANS curves shown in Figure 2a.

Solutions	Contour length (*L*) [Å]	Kuhn length (*b*) [Å]	Radius (*R*) [Å]	Polydispersity in radius
PBDTTT-C-T:$PC_{71}BM$/m-DCB	620 ± 8	107 ± 2	7.02 ± 0.83	0.34
PBDTTT-C-T/m-DCB	639 ± 8	111 ± 2	6.84 ± 0.90	0.34
PBDTTT-C-T:$PC_{71}BM$/m-DCB:DIO	620 ± 10	110 ± 3	6.70 ± 0.79	0.33
PBDTTT-C-T:m-DCB/DIO	630 ± 10	110 ± 3	6.67 ± 0.82	0.34

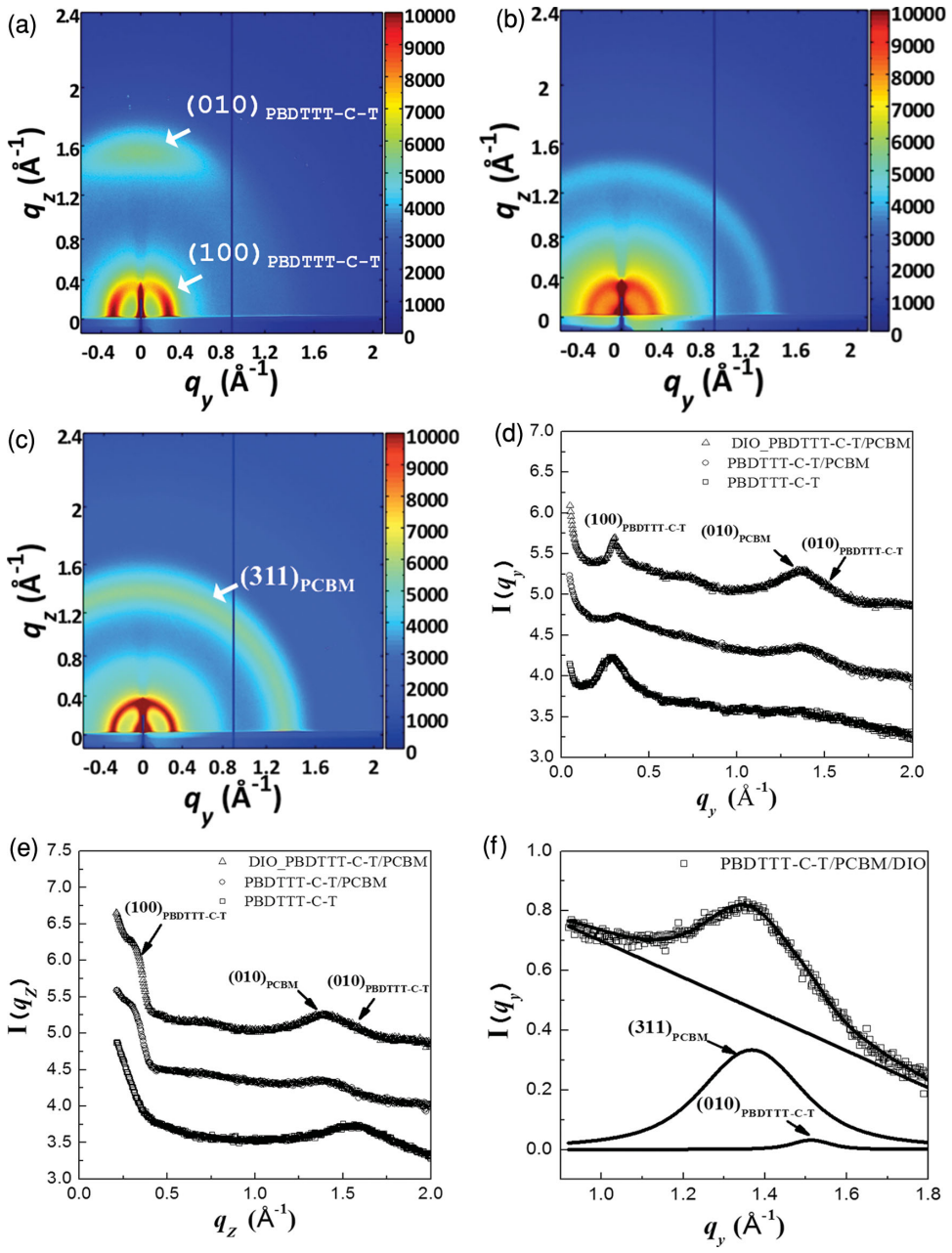

Figure 3. 2D GIWAXS patterns of a) pristine PBDTTT-C-T, b) PBDTTT-C-T: $PC_{71}BM$/DCB, and c) PBDTTT-C-T:$PC_{71}BM$/DCB:DIO film. d,e) in-plane and out-of-plane GIWAXS profiles extracted from the respective 2D GIWAXS patterns. f) A curve-fit result exemplifying the existence of (311) reflection of $PC_{71}BM$ and (100) of PBDTTT crystal.

found in the comparison between the 2D GIWAXS images of the blend films with and without DIO is that the PBDTTT-C-T:$PC_{71}BM$/DCB:DIO film exhibits stronger PBDTTT-C-T (100) and $PC_{71}BM$ (311) reflections implying a higher degree of crystallinity of the PBDTTT-C-T and $PC_{71}BM$. Enhanced crystallinity can be attributed to either an increased number of crystallites or larger crystal size. While the crystallinity is intensified by the DIO additive, there is no significant change of the (010) peak position, crystal size, or crystal orientation observed when processed with the DIO additive. It is well known that highly-crystalline morphologies will facilitate hole transport in the bulk film. Furthermore, recent studies reveal that the degree of crystallization is concurrent with phase segregation. The higher crystallinity of PBDTTT-C-T and $PC_{71}BM$ in the PBDTTT-C-T:$PC_{71}BM$/DCB:DIO film could also indicate an increased amount of available interfacial area between donors and acceptors that consequently resulted in enhanced charge separation. This is consistent with the observed significant increase of J_{sc} which results from both improved charge separation and transport. As hole transport through the PBDTTT-C-T percolating network is improved, balanced charge transport will also enhance the FF.

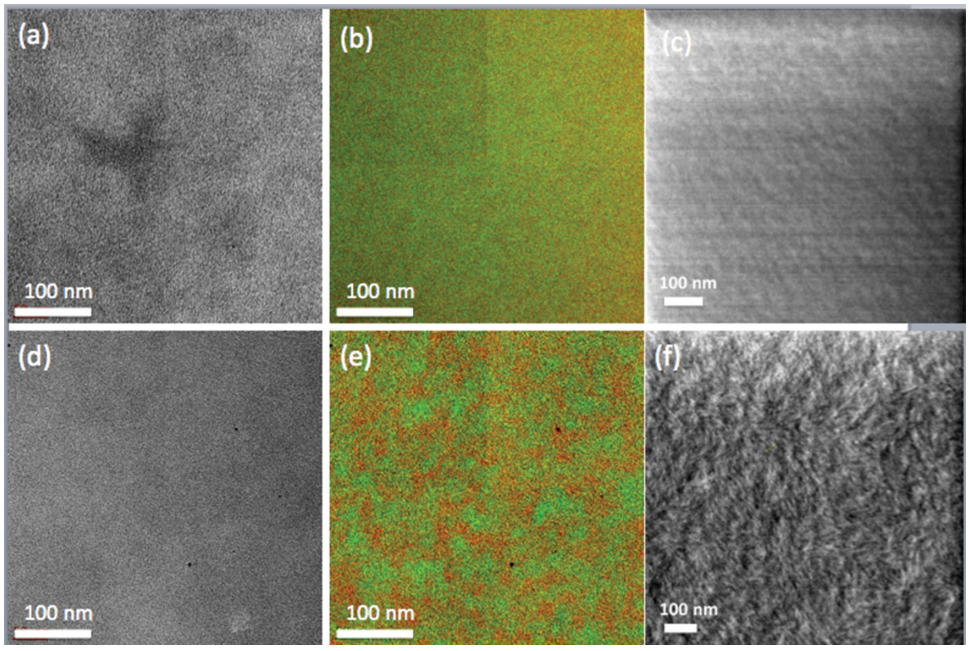

Figure 4. Morphology of BHJ films cast from PBDTTT-C-T:$PC_{71}BM$ without and with DIO processing solvent. a,b) EF-TEM images, and c) HIM image of PBDTTT-C-T:$PC_{71}BM$ film without DIO treatment; d,e) EF-TEM images, and f) HIM image of blend film with DIO. For EF-TEM images, each film was imaged at a,d) 0 ± 4 eV, b,e) 19 ± 4 eV and 30 ± 4 eV. The images taken at 19 eV and 30 eV were combined and presented using a colored scale (19 eV in red and 30 eV in green), where green represents the PBDTTT-C-T-rich domains and red the $PC_{71}BM$-rich domains.

This more evolved crystalline morphology of PBDTTT-C-T:$PC_{71}BM$/DCB:DIO film might be related to a plasticizing role of oligomeric DIO. Since DIO has a much higher boiling point (~269 °C) than DCB (~180 °C), DIO could be left in the film after the evaporation of DCB. The residual DIO might act as a plasticizer for the rearrangements of PBDTTT-C-T and $PC_{71}BM$. In this case, DIO could be embedded between the molecules in the film and could increase the free volumes to make the molecules more mobile. This would enable reaching their phase-segregated and crystalline state closer to equilibrium more easily with much-reduced molecular friction. Indeed, fast evaporation of solvent in spun-cast OPV blend films can trap the phase and crystalline morphology in transient states when the evaporation speed is comparable to phase-segregation and crystallization. Hence thermal or solvent vapor annealing has generally been applied to drive film crystalline morphologies closer to equilibrium.[5,6] When DIO is used, however, it has been shown that no such annealing is necessary.[15]

To better understand the effect of DIO on the phase separated morphology of PBDTTT-C-T:$PC_{71}BM$ blends, energy-filtered transmission electron microscopy (EF-TEM), AFM, and helium ion microscopy (HIM) were employed to investigate the polymer blend microstructures. First, the surface morphologies of PBDTTT-C-T:$PC_{71}BM$ blend films that were spun-cast from DCB and DCB/DIO solutions were imaged with AFM. The surface roughness of the film cast from DCB/DIO obviously increases compared to that from DCB as shown in Figure S2 (Supporting Information). As seen in the images, pronounced nanophase separation is observed in film cast from DCB/DIO but is barely detectable from pure DCB. These AFM observations are consistent with the morphologies imaged by both EF-TEM and HIM. This enhanced nanophase separation of PBDTTT-C-T:$PC_{71}BM$ in the DCB/DIO films may be a result of enhanced crystallization induced by the DIO. To compare the phase difference of the blends with and without DIO, the morphologies of the PBDTTT-C-T:$PC_{71}BM$ films with and without DIO treatment were also examined using low-voltage EF-TEM following a procedure reported in literature.[25] In **Figure 4**, the effect of the DIO additive on the morphology of the PBDTTT-C-T:$PC_{71}BM$ film was examined by EF-ETM with elastic energies of 0 ± 4 eV, 19 ± 4 eV, and 30 ± 4 eV. The contrast in elastic images is caused by electron density contrast. Nanofibril structures are visible in the 0 eV images for all the samples. Electron energy loss spectra (EELS) of pure donor and acceptor suggest that the donor has a low eV EELS peak around 17–22 eV, and acceptor has a peak around 26–32 eV, similar to what has been reported in the literature for other polymer donor/fullerene acceptor systems.[12] Therefore, we used 19 ± 4 eV to image donor-rich regions and 30 ± 4 eV to image acceptor-rich areas. The 19 eV image and the 30 eV image are essentially complementary and have been combined together to show the nanofibril-shaped donor-rich domains (colored green) and acceptor-rich matrix (colored red). The EF-TEM images of PBDTTT-C-T:$PC_{71}BM$ film cast from DCB consistently show the uniform, almost featureless contrast similar to the ones seen in AFM images, indicating a low degree of phase separation. This morphology is expected to result in inefficient exciton dissociation and it lacks the bicontinuous interpenetrating pathway necessary for the charge carriers to reach their respective electrodes. However, the EF-TEM images of PBDTTT-C-T:$PC_{71}BM$ film cast from DCB/DIO clearly demonstrate segregated donor- and acceptor-rich domains promoted by DIO. The different number of π and σ bonds in the polymer and PCBM result in minute changes of the secondary electron

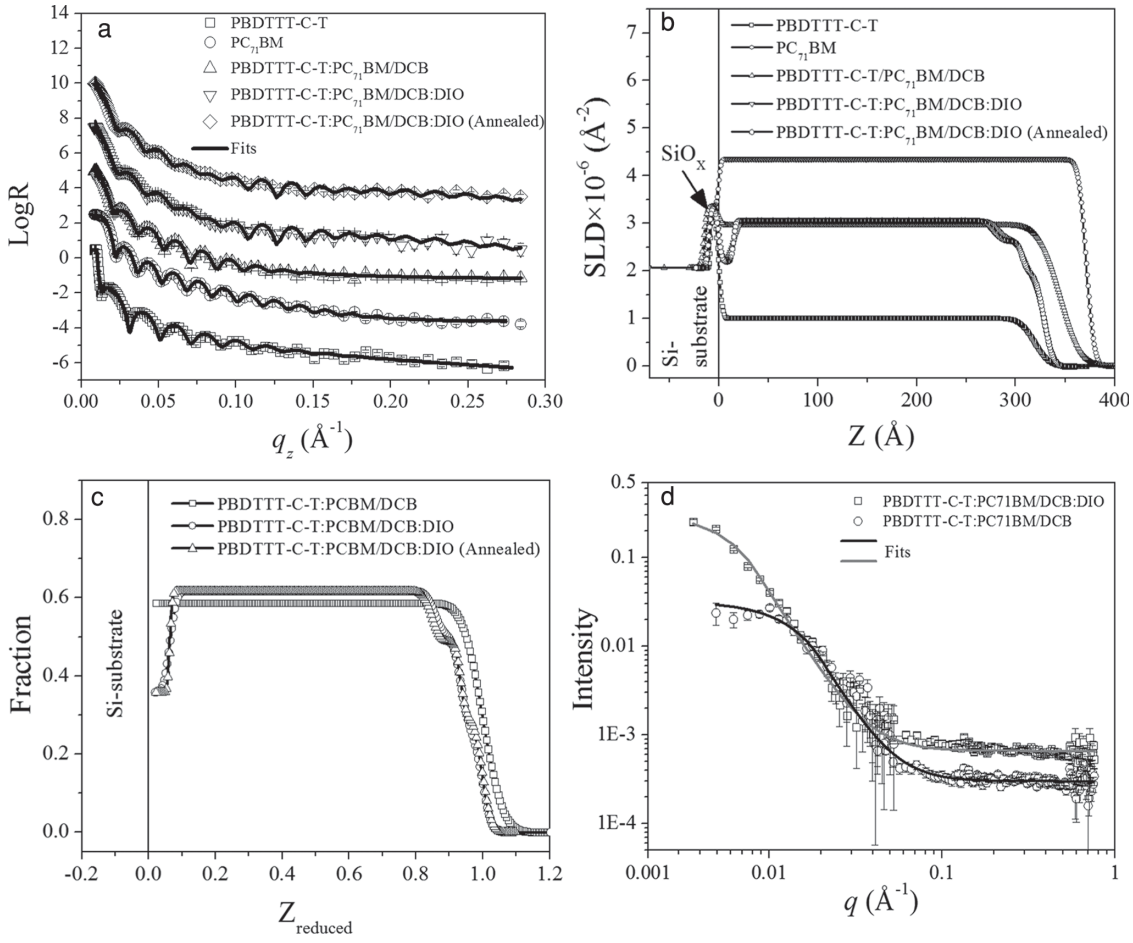

Figure 5. a) Experimental and modeled NR curves for PBDTTT-C-T, $PC_{71}BM$ PBDTTT-C-T:$PC_{71}BM$/DCB, PBDTTT-C-T:$PC_{71}BM$/DCB:DIO and annealed PBDTTT-CT:$PC_{71}BM$/ DCB:DIO film. The SLD profiles used to fit the NR curves shown in (b). Volume fraction profile of PCBM calculated from the SLD profiles shown in (c). Note that the SLD and ν_{PCBM} profiles of as-spun and annealed PBDTTT-C-T:$PC_{71}BM$/DCB:DIO film are nearly overlapped with minute difference. d) Guinier-Porod model fits to the SANS curves for PBDTTT-C-T:$PC_{71}BM$/DCB and PBDTTT-C-T:$PC_{71}BM$/DCB:DIO film.

yield in HIM,[26] which allows direct imaging of the phase separation morphology of the PBDTTT-C-T:$PC_{71}BM$ blend films as shown in Figures 4c and 4f. The HIM images again show evidence of phase separation with relatively bright and dark regions being present. The length scale of phase separation around 25 nm for the PBDTTT-C-T:$PC_{71}BM$ film cast from DCB/DIO appears much more pronounced than the samples cast from DCB. The lateral phase morphologies were further investigated on the PBDTTT-C-T:$PC_{71}BM$ films cast from DCB/DIO and DCB solutions onto glass slides by measuring SANS curves for the films in transmission geometry (**Figure 5**d). The SANS curves are fit using a Guinier-Porod model.[27,28] The obtained average radii of gyration (R_g) of the domains in the PBDTTT-C-T:$PC_{71}BM$ film cast from DCB:DIO and DCB are ≈25 and ≈11 nm, respectively. Due to the multiple scattering originating from the SLD contrasts between $PC_{71}BM$ and PBDTTT-C-T, and crystalline and amorphous PBDTTT-C-T, the average R_g obtained is associated with the average size of both PBDTTT-C-T crystals and aggregated $PC_{71}BM$ domains. However, since the SLD contrast between $PC_{71}BM$ and PBDTTT-C-T is much larger than that between crystalline and amorphous PBDTTT-C-T, the main scattering contribution is by $PC_{71}BM$. On the other hand, the higher scattered intensity of PBDTTT-C-T:$PC_{71}BM$ film cast from DCB:DIO as compared to PBDTTT-C-T:$PC_{71}BM$ film cast from DCB implies higher population of phase-separated domains. Also, the Porod exponents for the PBDTTT-C-T:$PC_{71}BM$/DCB:DIO and PBDTTT-C-T:$PC_{71}BM$/DCB film, that is, ≈3.1 and ≈3.2 indicates very rough fractal surface of the domains.[29] It should be noted here that the poor phase segregation of PBDTTT-C-T and $PC_{71}BM$ cast from DCB results in poor charge separation and charge transport, and hence, a low PCE is expected.

In order to further understand the effect of the DIO additive on the vertical profile of PBDTTT-C-T:$PC_{71}BM$ film, neutron reflectometry was employed to investigate the vertical distributions of the blending components. Figure 5a shows the experimental and fit neutron reflectivity (NR) curves for PBDTTT-C-T, $PC_{71}BM$, PBDTTT-C-T:$PC_{71}BM$ films cast from DCB and DCB:DIO solutions, where the measured NR curves are modeled using the Parratt formalism[30] to extract the vertical SLD profiles of films as shown in Figure 5b. The volume fraction profiles of $PC_{71}BM$ are obtained by using the method reported previously[31,32] and depicted in Figure 5c. As shown in Figure 5a, all the films exhibited Kiessig fringes, a

Table 3. Estimated χ_{ij} for different pairs along with their values (in parenthesis) at $T = 298$ K, relevant for this study.

Parameter	i = PBDTTT-C-T, j = $PC_{71}BM$	i = PBDTTT-C-T, j = DCB	i = PBDTTT-C-T, j = DIO	i = $PC_{71}BM$, j = DCB	i = $PC_{71}BM$, j = DIO	i = DCB, j = DIO
χ_{ij}	0.34 + 95.37/T (0.660)	0.34 + 0.15/T (0.341)	0.34 + 204.46/T (1.026)	0.34 + 33.48/T (0.452)	0.34 +431.65/T (1.788)	0.34 + 86.40/T (0.630)

characteristic of the interference of reflected neutrons. In the NR curves for the pristine PBDTTT-C-T and $PC_{71}BM$ films, single layer models with film thicknesses of ≈318 and ≈371 Å give rise to the best fits. The deduced SLDs for PBDTTT-C-T and $PC_{71}BM$ are 1.01×10^{-6} and 4.34×10^{-6} Å^{-2}, respectively. For the NR curve of PBDTTT-C-T:$PC_{71}BM$/DCB film, the best fit is achieved using a single layer model with a total thickness of ≈346 Å. This implies that the phase-separated $PC_{71}BM$ domains are distributed homogeneously through the thickness direction of the film. In the PBDTTT-C-T:$PC_{71}BM$/DCB:DIO film, however, the best fit is obtained using a 4-layer morphology, indicating that PBDTTT-C-T and $PC_{71}BM$ are distributed in different proportions through the thickness of the film. This result indicates that the DIO additive induce a strong vertical phase separation. Specifically, the results indicate that PCBM-depleted layers form preferentially at the top surface of the blend film formed with DCB/DIO, meaning that more polymers are enriched at the top interface. Our NR results agrees well with a very recent study that also showed that a solvent additive can modify the surface composition in BHJ films detected by other analysis techniques.[33] Moreover, annealing the PBDTTT-C-T:$PC_{71}BM$/DCB:DIO film at 150 °C (20 minutes) leads to essentially no change in the vertical phase morphology and film thickness beyond small changes in the roughness between the internal layers. This implies that no significant diffusion and rearrangement of PBDTTT-C-T and $PC_{71}BM$ occurs during the thermal annealing. An unchanged vertical phase morphology of the PBDTTT-C-T:$PC_{71}BM$:DIO bulk film upon thermal annealing suggest that the solvent additive DIO has already induced a stable and favorable film morphology close to equilibrium. Therefore, no extra post-processing step such as thermal annealing is required to further optimize the film morphology. In order to examine the diffusivity and miscibility of PBDTTT-C-T and $PC_{71}BM$, a bilayer film composed of a top PBDTTT-C-T layer and bottom $PC_{71}BM$ layer was prepared (see Supporting Information) and the bilayer film was annealed at 150 °C for 20 min. The NR results for the as-prepared and annealed bilayer film are shown in Figure S3. In the NR model fit for the as-prepared bilayer film, a 2-layer model was used from which the obtained SLDs for the top and bottom layer are identical to those obtained from pristine PBDTTT-C-T and $PC_{71}BM$ film shown in Figure 5c. However, annealing the bilayer film alters the neutron reflectivity pattern. The modified SLD distribution implies a rearrangement of PBDTTT-C-T and $PC_{71}BM$. It should be noted that, if PBDTTT-C-T and $PC_{71}BM$ are fully or partially miscible, and inter-diffusion should occur to increase the entropy of mixing, whereas, if not, the interfacial boundary would become sharper without inter-diffusion. From the neutron reflectivity results, it is evident that PBDTTT-C-T and $PC_{71}BM$ are miscible to some extent, even though the miscibility is much less significant as compared to that of poly(3-hexylhiophene) (P3HT) and $PC_{61}BM$.[31]

Based on the above comprehensive lateral and vertical structural film analyses resulting from the addition of DIO, a complete picture emerges for how the combination of resulting improvements in the crystallinity and phase morphology yields improved I_{sc}, FF and PCE of PBDTTT-C-T:$PC_{71}BM$ OPV. Improved crystalline structure and enhanced phase separation into larger scale and purer PBDTTT-C-T and $PC_{71}BM$ domains will facilitate the geminate charge carrier escape from the Coulumbic attraction, and meanwhile effectively lower the energy of the charge transfer states. The lowered charge transfer state will reduce charge carrier recombination into the triplet state of the polymer and exhibit a reduced V_{oc}, which is also observed in other polymer-fullerene BHJs upon using an additive.[34]

The effect of the solvent additive on the phase separation should strongly depend on the molecule interactions of the additive with the donor and acceptor during the evaporation process. In order to better understand the implications of solvent and additive evaporation on phase segregation, we have constructed a phase diagram for the four-component system (PBDTTT-C-T:PCBM:DCB:DIO) using Flory-Huggins theory.[35] Structural parameters for different molecules studied in this work are shown in Table S2. Estimated values of the Flory's χ_{ij} are presented in **Table 3**. A higher value of χ_{ij} signifies stronger repulsive interactions between i and j. Note that $\chi_{PBDTTT\text{-}C\text{-}T,PCBM} = 0.66$ implies that a binary blend of PBDTTT-C-T:PCBM will phase segregate for typical mixing ratios used in active layers of OPVs, as recently observed in molecular dynamics simulations.[36] The quaternary phase diagram computed using Flory-Huggins theory for the PBDTTT-C-T:$PC_{71}BM$:1,2-DCB:DIO system is presented in **Figure 6**a. The phase diagram highlights the different thermodynamic pathways to reach the same binary blend of PBDTTT-C-T and $PC_{71}BM$ (e.g., 40:60 as the volume ratio of PBDTTT-C-T:$PC_{71}BM$ in Figure 6a, depicted as a square). One path is along the solid arrow in the solvent-PCBM-polymer plane (i.e., DCB-PCBM-P plane in Figure 6a), where movement towards the binary blend state point is driven by solvent evaporation (note that in reality, solvent is evaporated from each coexisting phase and in turn becomes more concentrated). This particular path is followed in the absence of any solvent additive such as DIO. In the presence of solvent additive such as DIO, which is less volatile than the solvent (DCB), evaporation of the additive leads to the second path highlighted by the dashed arrow, until the system depletes all of the solvent. Further evaporation of DIO leads to movement along the dash-dotted arrow that reaches the binary blend of PBDTTT-C-T and $PC_{71}BM$. Note that these simple thermodynamic calculations highlight that the final stage is the same, independent of the presence or absence of solvent additives. This indicates that kinetic processes (such as evaporation rates) are important to differentiate the morphological differences observed in the experiments.

The experimental system studied in this work, with 10 mg mL^{-1} of PBDTTT-C-T mixed with 15 mg mL^{-1} of

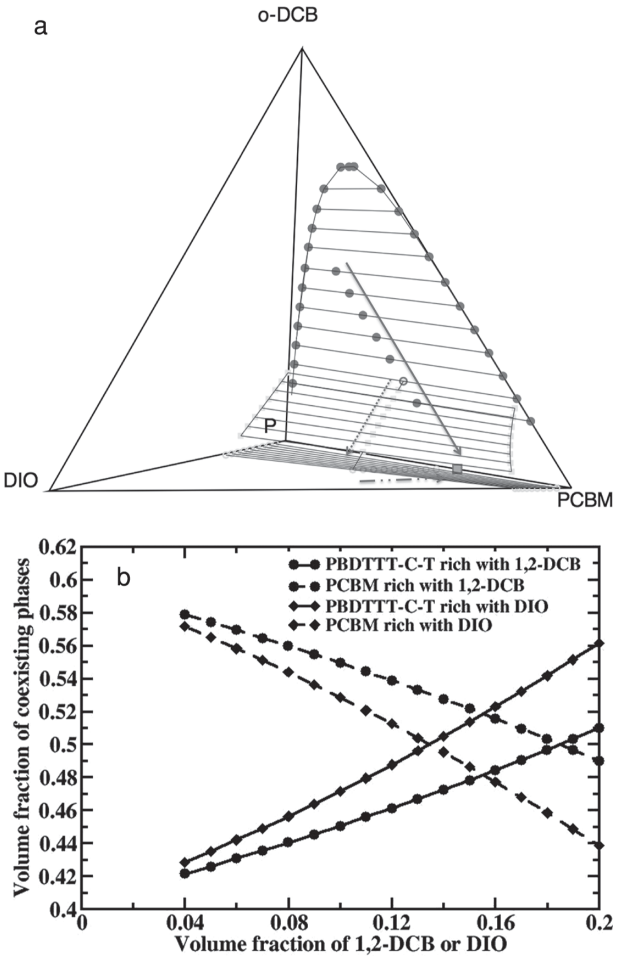

Figure 6. a) Phase diagram for the PBDTTT-C-T:$PC_{71}BM$:DCB:DIO system constructed using Flory-Huggins theory. In this figure, the label P represents PBDTTT-C-T and the blue lines represent the tie lines. b) Volume fraction of coexisting phases as the residual solvent (DCB) or the additive (DIO) evaporates as obtained from Flory-Huggins theory for a ternary system containing 40% PBDTTT-C-T by volume. It is clear from the phase diagram how trace amounts of DIO or DCB can lead to significant differences in the volume fractions of the coexisting phases.

$PC_{71}BM$, corresponds to 0.00017 (for $N = 25$) and 0.00874 as volume fraction for the PBDTTT-C-T and $PC_{71}BM$, respectively, using molar volumes given in Table S2 (Supporting Information). Such a dilute system (even with DIO) corresponds to a point close to the apex in Figure 6a and should be a stable one-phase system, which is in agreement with the SANS results, where no sign of phase segregation is observed in the casting film from the solution with and without DIO. Figure 6b shows volume fractions of each coexisting phase as a function of the residual DCB or the DIO remaining in the system for the case containing 40% PBDTTT-C-T by volume. The observed difference is an outcome of the higher values of the Flory's chi parameters for interactions involving DIO in contrast to DCB (cf. Table 3). DIO or DCB evaporation leads to movement of the interface between the coexisting phases in such a way that the volume fraction of each phase is given by Figure 6b and as a result the relative size of the domains changes. It should be clear from Figure 6b that the domain size depends on the residual volume fraction of DCB or DIO and the volume fraction of PBDTTT-C-T and $PC_{71}BM$ in the final blend. Also note that in the absence of a quantitative description of the solvent evaporation rates on the morphology, the experimentally observed enhanced phase segregation in the presence of DIO may be due to the role played by different evaporation rates of DIO and DCB. We plan to address this issue in a future publication.

Based on the above structure information and theoretical calculations, we propose a schematic morphology evolution of PBDTTT-C-T: $PC_{71}BM$ BHJ in the film forming from the solution phase containing solvent additive. Also, we qualitatively compare our results with a similar system consisting of PTB7:$PC_{71}BM$:DCB in solution phase. Although both PBDTTT-C-T and PTB7 contain benzo[1,2-b:4,5-b']dithiophene (BDT) and thieno[3,4-b] thiophene (TT) units on the backbone, these polymers differ in side groups. PBDTTT-C-T has alkylthienyl side groups in contrast to alkoxy in PTB7 and exhibit higher molecular planarity. These differences in chemical structures manifest in molecular interactions and in turn, physical properties. For example, the alkylthienyl side groups in PBDTTT-C-T lead to two-dimensional conjugation in contrast to PTB7. Also, due to the enhanced π interaction with $PC_{71}BM$, PBDTTT-C-T has better molecular miscibility with $PC_{71}BM$ than PTB7.

Our SANS study in solution revealed that PBDTTT-C-T and PCBM are both well dissolved in DCB, showing no signature of aggregation. In addition, trace amounts of DIO do not affect the structure in a significant manner. Note that our SANS results are different from the work by Lou et al. on PTB7:$PC_{71}BM$:DCB solution, where it was shown that the DIO breaks up $PC_{71}BM$ aggregates into small clusters. Such an effect of DIO on the structure in solution can be attributed to different molecular structures as discussed above and the resulting disparate interaction parameters for PBDTTT-C-T and PTB7, which results in different solubility, crystallization ability and miscibility with PCBM. Furthermore, our neutron reflectivity results (Figure S3, Supporting Information) have shown that PBDTTT-C-T is miscible with $PC_{71}BM$, which is in in striking disagreement with behavior of PTB7:$PC_{71}BM$ system and agreement with our SANS study.

We envision that different sizes of fullerene aggregates in the initial state would have very important effects on phase aggregation in film formation. We hypothesize that in our case, the uniform dispersion of PBDTTT-C-T and $PC_{71}BM$ does not provide favorable nuclei sites for crystallization as the solvent evaporates. This eventually produces a fine intermixing between PBDTTT-C-T and fullerene in the BHJ formation stage of the film. On the contrary, the pre-aggregated fullerene molecules in the PTB7:$PC_{71}BM$:DCB solution can act as nuclei sites to facilitate the fast growth of fullerene aggregates during the film formation process. Hence, oversized fullerene domains on the length scale of hundreds of nanometers are observed in the PTB7:$PC_{71}BM$ film without additive processing. In our PBDTTT-C-T: $PC_{71}BM$ blend, $PC_{71}BM$ completely inhibits the crystallization of polymer because of the good miscibility between PBDTTT-C-T and $PC_{71}BM$ in the DCB solution. However, lubricant DIO molecule appear to act as a "plasticizer" to facilitate the polymer chain re-organization. Eventually, the PCBM molecules aggregate into larger PCBM clusters, and consequently increase the fullerene domain size. In contrast,

for the case of PTB7:$PC_{71}BM$:DCB, the fullerene cannot completely suppress the polymer crystallization because of comparably worse miscibility between PTB7 and $PC_{71}BM$. Therefore, smaller aggregated domains already exist in the initial state. During the drying process, these polymer domains grow along with aggregation of fullerenes approaching a length scale as large as hundreds of nanometers. When processed with solvent additives, the high-boiling point DIO retards the drying process. Consequently, larger PTB7 rich domains form and confine the PCBM into smaller aggregated domains, leading to a fibra-like morphology with reduced fullerene domain size.[37] In both cases, the final domain sizes of polymer and fullerene are around 20–30 nm which ensures the efficient charge separation at the donor-acceptor interface and carrier transport through the bi-continuous network.

3. Conclusion

A comprehensive suite of characterization techniques and theoretical analyses were used to reveal both the lateral and vertical morphological effects of an additive, DIO, on the formation of BHJs and the resulting OPV device parameters starting from a donor/acceptor polymer blend PBDTTT-C-T:$PC_{71}BM$ in solution, to the spin-cast films. SANS of the casting solutions indicated that both PBDTTT-C-T and $PC_{71}BM$ were well-dissolved in both pristine DCB and DCB/DIO, and showed that the DIO additive did not affect their aggregation in solution. However, DIO was found to play a very important role in the morphological evolution of the film during solidification, resulting in enhanced crystallinity, and strongly-enhanced lateral and vertical phase separation observed between the PBDTTT-C-T:$PC_{71}BM$ domains in the BHJ film. These morphological improvements resulting from the addition of DIO were consistent with the measured changes in OPV device parameters resulting in enhanced PCE.

A thermodynamic analysis based on Flory-Huggins theory for this experimentally-studied system verified the absence of phase segregation in the solution phase and revealed how small changes in additive concentration can result in significant changes in volume fractions of the coexisting phases. Based on this thermodynamic description, we attribute the observed morphological effects of DIO in the experiments to result from a) trace amounts of DIO or the DCB remaining in the films, or b) kinetic effects resulting from the different evaporation rates of DCB and DIO. The plasticizing effect of the low-viscosity DIO, paired with its much lower evaporation rate than DCB, may be responsible for the increased diffusivity of PBDTTT-C-T and $PC_{71}BM$ during DCB evaporation and the observed enhanced crystallization and phase-segregation.

4. Experimental Section

Devices Fabrication and Testing: The PBDTTT-C-T was synthesized using previously reported procedures. $PC_{71}BM$ was purchased from Nano-C Inc. The blends with 1:1.5 wt% PBDTTT-C-T:$PC_{71}BM$ ratio were dissolved in DCB at a concentration of 25 mg mL^{-1}. BHJ OPV devices with the layer structure of ITO/PEDOT:PSS/PBDTTT-C-T:$PC_{71}BM$/Ca/Al were fabricated as follows. ITO substrates were first cleaned by ultrasonic agitation in detergent, DI water, acetone and isopropyl alcohol (IPA). The cleaned ITO substrates were then treated with UV ozone for 20 min. PEDOT:PSS was spin-coated on the cleaned ITO substrates and baked for 1 hour at 120 °C. For a complete dissolution of PBDTTT-C-T and $PC_{71}BM$, the solutions were heated on a hotplate overnight at 50 °C. 3% of DIO was added to the PBDTTT-C-T:$PC_{71}BM$/DCB solutions prior to the spin-coating. The blend solutions were then spin-coated on the PEDOT:PSS-coated substrates at a spinning speed of 900 rpm. Lastly, Ca and Al were coated on top of the PBDTTT-C-T:$PC_{71}BM$ layers through a shadow mask by the thermal evaporation. Current-voltage characterization of the prepared OPVs were conducted by a Keithley 4200 semiconductor parameter analyzer under the AM 1.5 conditions (100 mW cm^{-2}).

Solution and Thin Film Characterization: SANS measurements for the casting solutions were conducted at the General Purpose-SANS beamline (CG-2) at the High-Flux Isotope Reactor (HFIR) and the Spallation Neutron Source (SNS), Oak Ridge National Laboratory (ORNL). In the measurements, two configurations with different neutron wavelengths/sample-to-detector distances, that is, 4.75 Å/4.9 m and 12 Å/19.4 m were chosen. 10 mg/ml, 15 mg/ml and 25 mg/ml concentration PBDTTT-C-T, PCBM and PBDTTT-C-T:PCBM (1:1.5) solutions, and the corresponding solvents were loaded into 1mm-thick quartz cells and the scattered beams were collected at each SANS configuration. The raw 2D SANS data were corrected for detector response, dark current and scattering from background, before being azimuthally averaged to produce the 1D SANS profiles, that is, $I(q)$ versus q profile. The data were placed on an absolute scale (cm^{-1}) by the use of measured direct beam. PBDTTT-C-T:$PC_{71}BM$/DCB and PBDTTT-C-T:$PC_{71}BM$/DCB:DIO solution were spun-cast onto glass slides to prepare films for transmission SANS measurements. In order to increase the counting statistics, 5 of those films were stacked and placed perpendicular to the incident neutron beam. The SANS measurements were performed at the EQ-SANS instrument in the SNS, ORNL using 60 Hz operation. Three configurations with different sample-to-detector distance of 4 m, 2.5 m, and 1.3 m and two different neutron wavelength bands were used. The measured scattering intensity was corrected for detector sensitivity and the background scattering, and placed on an absolute scale using a calibrated standard. All the SANS measurements were carried out using quartz cells with 1 mm path length at room temperature (25 °C). In the SANS measurements, scattered neutrons were collected using a 2D position sensitive ^{3}He detector with 1 m × 1 m active area, composed of tube detectors providing 256×192 pixels. Neutron reflectivity data were collected on the Liquids Reflectometer (Beamline-4B) at the SNS, ORNL. NR data were collected using a neutron beam with a bandwidth of 3.5 Å (2.5 Å < λ < 6.0 Å), where λ is the wavelength of incident neutron. The reduced data were in the format of absolute neutron reflectivity (R) vs. neutron momentum transfer (q_z), where $q_z = (4\pi/\lambda)\sin\alpha_i$ with α_i being the incidence angle of neutron beam. In order to account for the instrumental smearing of NR data, the instrumental resolution provided from the beamline was convolved with the calculated NR curves. UV–Vis absorption sepectrascopy was recorded using a Varian Cary UV–Vis–NIR spectrophotometer. Atomic force microscope (AFM) images were acquired with a Bruker Dimension Icon operating in a tapping mode. Transmission Electron Microscopy (TEM) investigation were performed using a Zeiss Libra 120 with an in-column energy filter at 120 keV after floating the active layer on deionized water surface and subsequent picking-up with a 400-mesh or 600-mesh copper grid. Grazing incidence X-ray scattering (GIXS) profiles were measured on the beamline 8ID-E at the Advanced Photon Source (APS), Argonne National Laboratory (ANL). Here, q_y and q_z are the in-plane and out-of-plane scattering vectors, respectively. q_y and q_z are given by $q_y = 2\pi/\lambda_X[\sin(\psi)\cos(\alpha_f)]$ and $q_z = 2\pi/\lambda_X[\sin(\alpha_i)\sin(\alpha_f)]$, where λ_X, α_i, α_f, and ψ are the wavelength, out-of-plane exit angle and in-plane exit angle of X-ray beam, respectively.

Supporting Information

Supporting Information is available from the Wiley Online Library or from the author.

Acknowledgements

M.S. and J.K. contributed equally for this work. This research was conducted at the Center for Nanophase Materials Sciences (CNMS), High Flux Isotope Reactor (HFIR) and Spallation Neutron Source (SNS) which are sponsored at Oak Ridge National Laboratory by the Office of Basic Energy Sciences, U.S. Department of Energy. KX and DBG acknowledge the support provided by a Laboratory Directed Research and Development award from the Oak Ridge National Laboratory (ORNL) for the neutron experiments.

Received: May 13, 2014
Revised: July 15, 2014
Published online: August 26, 2014

[1] M. A. Green, K. Emery, Y. Hishikawa, W. Warta, E. D. Dunlop, *Prog. Photovoltaics* **2013**, *21*, 827.
[2] G. Li, R. Zhu, Y. Yang, *Nat. Photonics* **2012**, *6*, 153.
[3] Y. Y. Liang, Z. Xu, J. B. Xia, S. T. Tsai, Y. Wu, G. Li, C. Ray, L. P. Yu, *Adv. Mater.* **2010**, *22*, E135.
[4] L. J. Huo, S. Q. Zhang, X. Guo, F. Xu, Y. F. Li, J. H. Hou, *Angew. Chem. Int. Ed.* **2011**, *50*, 9697.
[5] W. L. Ma, C. Y. Yang, X. Gong, K. Lee, A. J. Heeger, *Adv. Funct. Mater.* **2005**, *15*, 1617.
[6] F. Padinger, R. S. Rittberger, N. S. Sariciftci, *Adv. Funct. Mater.* **2003**, *13*, 85.
[7] G. Li, V. Shrotriya, J. S. Huang, Y. Yao, T. Moriarty, K. Emery, Y. Yang, *Nat. Mater.* **2005**, *4*, 864.
[8] F. L. Zhang, K. G. Jespersen, C. Bjorstrom, M. Svensson, M. R. Andersson, V. Sundstrom, K. Magnusson, E. Moons, A. Yartsev, O. Inganas, *Adv. Funct. Mater.* **2006**, *16*, 667.
[9] M. M. Wienk, M. Turbiez, J. Gilot, R. A. J. Janssen, *Adv. Mater.* **2008**, *20*, 2556.
[10] C. S. Kim, L. L. Tinker, B. F. DiSalle, E. D. Gomez, S. Lee, S. Bernhard, Y. L. Loo, *Adv. Mater.* **2009**, *21*, 3110.
[11] Z. Z. Sun, K. Xiao, J. K. Keum, X. Yu, K. L. Hong, J. Browning, I. N. Ivanov, J. H. Chen, J. Alonzo, D. W. Li, B. G. Sumpter, E. A. Payzant, C. M. Rouleau, D. B. Geohegan, *Adv. Mater.* **2011**, *23*, 5529.
[12] J. H. Chen, X. Yu, K. L. Hong, J. M. Messman, D. L. Pickel, K. Xiao, M. D. Dadmun, J. W. Mays, A. J. Rondinone, B. G. Sumpter, S. M. Kilbey, *J. Mater. Chem.* **2012**, *22*, 13013.
[13] H. C. Liao, C. C. Ho, C. Y. Chang, M. H. Jao, S. B. Darling, W. F. Su, *Mater. Today* **2013**, *16*, 326.
[14] J. K. Lee, W. L. Ma, C. J. Brabec, J. Yuen, J. S. Moon, J. Y. Kim, K. Lee, G. C. Bazan, A. J. Heeger, *J. Am. Chem. Soc.* **2008**, *130*, 3619.
[15] J. Peet, J. Y. Kim, N. E. Coates, W. L. Ma, D. Moses, A. J. Heeger, G. C. Bazan, *Nat. Mater.* **2007**, *6*, 497.
[16] X. Guo, C. H. Cui, M. J. Zhang, L. J. Huo, Y. Huang, J. H. Hou, Y. Li, *Energy Environ. Sci.* **2012**, *5*, 7943.
[17] Y. M. Sun, G. C. Welch, W. L. Leong, C. J. Takacs, G. C. Bazan, A. J. Heeger, *Nat. Mater.* **2012**, *11*, 44.
[18] S. J. Lou, J. M. Szarko, T. Xu, L. P. Yu, T. J. Marks, L. X. Chen, *J. Am. Chem. Soc.* **2011**, *133*, 20661.
[19] K. Schmidt, C. J. Tassone, J. R. Niskala, A. T. Yiu, O. P. Lee, T. M. Weiss, C. Wang, J. M. J. Frechet, P. M. Beaujuge, M. F. Toney, *Adv. Mater.* **2013**, *26*, 300.
[20] D. Di Nuzzo, A. Aguirre, M. Shahid, V. S. Gevaerts, S. C. J. Meskers, R. A. J. Janssen, *Adv. Mater.* **2010**, *22*, 4321.
[21] W. W. Li, Y. Zhou, B. V. Andersson, L. M. Andersson, Y. Thomann, C. Veit, K. Tvingstedt, R. P. Qin, Z. S. Bo, O. Inganas, U. Wurfel, F. L. Zhang, *Org. Electron.* **2011**, *12*, 1544.
[22] V. F. Sears, *Neutron News* **1992**, *3*, 26.
[23] W. R. Chen, P. D. Butler, L. J. Magid, *Langmuir* **2006**, *22*, 6539.
[24] J. S. Pedersen, P. Schurtenberger, *Macromolecules* **1996**, *29*, 7602.
[25] L. F. Drummy, R. J. Davis, D. L. Moore, M. Durstock, R. A. Vaia, J. W. P. Hsu, *Chem. Mater.* **2011**, *23*, 907.
[26] A. J. Pearson, S. A. Boden, D. M. Bagnall, D. G. Lidzey, C. Rodenburg, *Nano Lett.* **2011**, *11*, 4275.
[27] B. Hammouda, *J. Appl. Crystallogr.* **2010**, *43*, 716.
[28] J. K. Keum, K. Xiao, I. N. Ivanov, K. L. Hong, J. F. Browning, G. S. Smith, M. Shao, K. C. Littrell, A. J. Rondinone, E. A. Payzant, J. H. Chen, D. K. Hensley, *Cryst. Eng. Commun.* **2013**, *15*, 1114.
[29] O. Glatter, O. Kratky, *Small-Angle X-ray Scattering*, Academic Press, London **1982**.
[30] L. G. Parratt, *Phys. Rev.* **1954**, *95*, 359.
[31] J. K. Keum, J. F. Browning, K. Xiao, M. Shao, C. E. Halbert, K. L. Hong, *Appl. Phys. Lett.* **2013**, *103*, 223301.
[32] A. J. Clulow, A. Armin, K. H. Lee, A. K. Pandey, C. Tao, M. Velusamy, M. James, A. Nelson, P. L. Burn, I. R. Gentle, P. Meredith, *Langmuir* **2014**, *30*, 1410.
[33] X. Z. Guo, M. Zhang, W. Ma, L. Ye, S. Zhang, S. Liu, H. Ade, F. Huang, J. Hou, *Adv. Mater.* **2014**, *26*, 4043.
[34] D. D. Nuzzo, A. Aguirre, M. Shahid, V. S. Gevvaerts, S. C. J. Mesker, R. A. J. Jassen, *Adv. Mater.* **2010**, *22*, 4321.
[35] P. J. Flory, *Principles of Polymer Chemistry*, Cornell University Press, New York **1953**.
[36] J. M. Y. Carrillo, R. Kumar, M. Goswami, B. G. Sumpter, W. M. Brown, *Phys. Chem. Chem. Phys.* **2013**, *15*, 17873.
[37] G. J. Hedley, A. J. Ward, A. Alekseev, C. T. Howells, E. R. Martins, L. A. Serrano, G. Cooke, A. Ruseckas, I. D. W. Samuel, *Nat. Commun.* **2013**, *4*, 2867.